PCCP

Diffusion of Ferrocene through Vanadyl Phosphate by Density Functional Theory

Journal:	*Physical Chemistry Chemical Physics*
Manuscript ID	CP-ART-06-2024-002433.R1
Article Type:	Paper
Date Submitted by the Author:	30-Jul-2024

Complete List of Authors:	Liu, Yuan; University of Florida, Ta, An; University of Florida, Ullberg, Seaton; University of Florida Liu, Jiahui; University of Florida Talham, Daniel R.; University of Florida Simon, Phillpot; University of Florida, Department of Materials Science and Engineering

Diffusion of Ferrocene through Vanadyl Phosphate by Density Functional Theory

Yuan Liu (刘源)[1†], An T. Ta[1], R. Seaton Ullberg[1], Jiahui Liu[2], Daniel R. Talham[2] and Simon R. Phillpot[1*]

[1]Department of Materials Science and Engineering, University of Florida, Gainesville FL 32611 USA

[2]Department of Chemistry, University of Florida, Gainesville FL 32611 USA

To be submitted to Physical Chemistry Chemical Physics

Abstract

Here, we employed the Nudged Elastic Band (NEB) method to simulate the diffusion of ferrocene through vanadyl phosphate ($VOPO_4$), with a focus on understanding the diffusion pathways arising from the complex structure of ferrocene. We systematically evaluated a total of 36 potential diffusion paths, categorizing them into three groups based on their directional orientation: 15 paths between V sites along the [110] direction, 15 paths from V to P sites along the [100] direction, and 6 paths between P sites also along the [110] direction. Our analysis revealed that the energy barriers for diffusion along the [110] direction typically ranged between 0.25 and 0.35 eV, which are notably higher than those observed for pathways along the [100] direction, where the energy barriers ranged from 0.11 to 0.20 eV. To further elucidate the complex deformation of ferrocene during diffusion, we established four key measures to characterize the structural conformation: the angle of the axis of the ferrocene molecule relative to the [010] direction within the (001) plane, the dihedral angle between the two cyclopentadienyl rings, the orientation angle of the -CH bonds with respect to the [001] direction, and the angle between two -CH bonds from the two cyclopentadienyl rings.

Key words: vanadyl phosphate, ferrocene, nudged elastic band, diffusion.

† Current address: Primera Analytical Solutions, Princeton NJ

* Corresponding author: sphil@mse.ufl.edu

ORCIDS: YL: 0000-0003-3973-4207; AT: 0000-0002-2767-8343; RSU: 0000-0001-5138-1833; JL: 0009-0008-9444-7175; DRT: 0000-0003-1783-5285; SRP: 0000-0002-7774-6535

1. Introduction.

Vanadyl phosphate ($VOPO_4$), a versatile inorganic compound known for its layered crystal structure,[1,2] has garnered significant attention for energy storage systems.[3–5] This interest is driven by its unique properties, including its ability to host a variety of intercalants between its layers. The process of intercalating ions and molecules into $VOPO_4$ not only modifies its intrinsic electrical and structural characteristics, but also tailors its performance for specific applications,[6–8] such as in batteries[9–14] and catalytic systems.[15–21]

Intercalation involves the reversible insertion of guest species (ions or molecules) into a host material without causing substantial disruption to its lattice structure.[22–25] In the case of $VOPO_4$, this process is of particular interest for enhancing ion transport and electronic conductivity, crucial for high-performance electrochemical devices.[7] Among various potential intercalants, the integration of metallic ions such as lithium[8,13,26–30] or sodium[31–36] has been extensively studied for battery applications. At the same time, the intercalation of molecular species presents an opportunity to generate hybrid materials. Metallocenes, a class of organometallic compounds consisting of two cyclopentadienyl anions bound to a metal center in a sandwich configuration, are a common choice of guest because they are relatively easily oxidized and undergo minimal structural reorganization. Metallocene intercalation[1,8,25,37–40] into layered hosts is studied as a route to new materials, but also because the well-behaved guest provides a handle to interrogate fundamentals of intercalation processes.

Therefore, a detailed understanding of the intercalation and diffusion mechanisms of ferrocene into vanadyl phosphate will be of great value. In this work, we elucidate the diffusion mechanisms using the Nudged Elastic Band (NEB) methods in Density Functional Theory (DFT). We recall the stable configuration of ferrocene within the $VOPO_4$ matrix, determined by DFT in a previous work.[41] Subsequently, the NEB method is applied to determine the most favorable pathways for the ferrocene's

movement. This approach offers a detailed picture of the energy barriers to diffusion and viable diffusion pathways for ferrocene.

2. Computational Method and Structures.

2.1 Computational methods

The DFT computations in this research were conducted using the Vienna Ab-initio Simulation Package (VASP), [42,43] leveraging the Perdew-Burke-Ernzerhof (PBE) exchange-correlation functional within the Generalized Gradient Approximation (GGA).[44] The methodology employed projector-augmented wave (PAW)[45,46] pseudopotentials for the elements involved. Specifically, the valence electron configurations were as follows: vanadium ($3d^4 4s^1$) with five valence electrons, phosphorus ($3s^2 3p^3$) with five, iron ($3d^7 4s^1$) with eight, oxygen ($2s^2 2p^4$) with six, and carbon ($2s^2 2p^2$) with four. A plane-wave cut-off energy of 600 eV was set to ensure the convergence of the calculations.

To address electron localization effects, particularly in the 3d states of vanadium, the DFT+U[47] method was incorporated, applying a U value of 3.25 eV to V[28,48] Furthermore, to enhance the treatment of van der Waals forces, the DFT+D3[49,50] correction was integrated into the calculations.

Optimization of atomic structures was achieved through the conjugate gradient method,[51,52] proceeding until the average force on atoms was reduced to below 0.025 eV/Å. To guarantee precision, the energy tolerance for electronic steps was set to 1×10^{-6} eV. Spin polarization was accounted for in all computational steps to capture magnetic interactions, and Gaussian smearing, with a width of 0.05 eV, was utilized to aid in the optimization process.

The Climbing Image Nudged Elastic Band (CI-NEB) was used to determine diffusion paths and energy barriers. These calculations were performed using the VTST tools, with an energy tolerance set at 0.03 eV/Å.[53,54] The Quick-Min method served as

the optimizer,[55] utilizing default parameters. Tests for k-mesh density and the number of image insertions are detailed in Section 3.1. To verify that the springs between the images in the NEB have no significant effect on the results, various spring constants were explored, see Figure S1 in SI. CrystalMaker was used to visualize the structures.[56] Finally, we used VASPKIT[57] to insert the images along the diffusion path.

2.2 Diffusion paths.

In our previous studies,[41] we identified five distinct configurations of ferrocene on the V/VO site: E-V-0º, E-V-45º, E-VO-0º, E-VO-45º, and S-V-45º. Here, 'E' denotes an eclipsed arrangement of ferrocene, while 'S' indicates a staggered arrangement. This structural arrangement arises as the vanadium square pyramids within the layers are aligned such that a ferrocene molecule in the interstitial region interacts with a vanadyl oxygen atom on one plane (VO site) and with the base of the square pyramid on the alternate plane (V site). The notation 'V' refers to the apical hydrogen directed from the cyclopentadienyl ring face towards the V side, and 'VO' indicates the apex facing the VO side. The numbers 0º and 45º represent the axis of the ferrocene from one cyclopentadienyl ring to the other through the Fe, being parallel to the [010] and [110] directions, respectively. As examples, Figures 1a) and a') showing the E-V-45º configuration. The other four configurations of the ferrocene on the V site are shown Figure S2 in the SI. Additionally, it is important to note that the c lattice parameter increases from 4.285 Å to 9.737 Å due to ferrocene intercalation, and these values agree with the experimental values in pristine (4.22 Å)[58] and Fc-$VOPO_4$ systems (9.79 Å).[25]

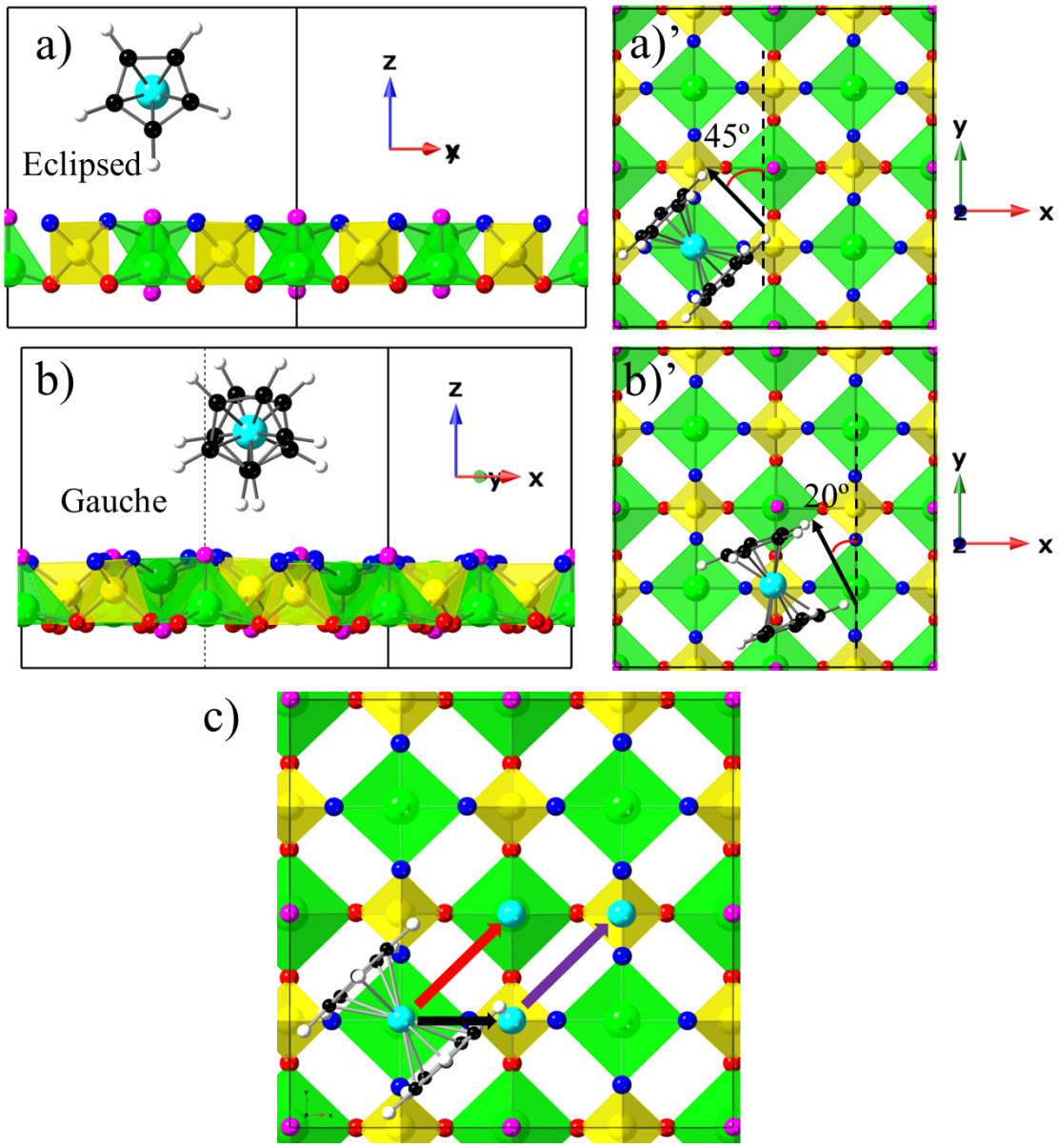

Figure 1. a) E-V-45º configuration viewed along [-110] direction and a)' along [001] direction; b) G-P-20º configuration viewed along [-120] direction and b)' along [001] direction. Vanadium is represented in green and coordinated in a pentagonal pyramidal geometry as part of a VO_5 complex; Phosphorus is shown in yellow and coordinated in a tetrahedral geometry as part of a PO_4 complex; The oxygen atoms are color-coded based on their position: the apical oxygen in the VO_5 pyramid is pink, those on the lower side of the layers (-z) are red, and the oxygen atoms on the upper side of the layers are blue; iron is cyan, carbon is black and hydrogen is white. The black lines show the edges of the supercell; c) illustration of the three ferrocene diffusion directions considered: the black arrow represents movement from the V site to the P site along the

[100] direction; the red arrow signifies ferrocene moving from one V site to another along the [110] direction; the purple arrow depicts movement from one P site to another along the [100] direction. Carbon and hydrogen atoms are omitted for clarity.

For the ferrocene sitting on top of a P site, we identified three configurations: E-Pv-0º, E-Pvo-0º, and G-P-20º. 'Pvo' denotes that the direction of the apical hydrogen at the P site is the same as in the E-VO configuration, while 'Pv' indicates a configuration with the apical hydrogen corresponding to the E-V configuration. 'G' signifies a gauche arrangement, which is an intermediate state between eclipsed and perfect staggered arrangements. The 20º means the ferrocene lies at 20º to the [010] direction. Figures 1b) and b') show the G-P-20º case; the other two configurations are shown in Figure S2 in the SI.

In an earlier paper,[41] we compared the total energy of various configurations and found that the E-V-45º configuration exhibits the lowest energy. This was attributed to differences in charge density between vanadium and iron, coupled with stronger van der Waals interactions between the apical hydrogen and oxygen from the vanadyl group. On the P/P site, the configuration with the lowest energy was identified as G-P-20º, though it had a slightly higher energy (+0.082 eV) than the E-V-45º configuration.

We also found that the bandgap of the Fc-$VOPO_4$ system is reduced compared to pristine $VOPO_4$, decreasing from 2.5 eV to 0.5 eV (see the density of states in Figure S3 in SI). In pristine $VOPO_4$, the highest occupied molecular orbital (HOMO) is dominated by the O-p orbital and the lowest unoccupied molecular orbital (LUMO) is dominated by the V-d orbital. However, in the Fc-$VOPO_4$ system, the intercalation of ferrocene introduces new states from the Fe-d orbitals near the Fermi level, leading to the bandgap reduction. This reduction in bandgap and the increased density of states at the Fermi level imply enhanced electronic conductivity, which could be advantageous for various electronic and electrochemical applications.

In this work, we consider three possible diffusion paths for the ferrocene: (i) from a V/VO site to a P/P site, along the [100] direction, (ii) from a V/VO to another V/VO, along the [110] direction, and (iii) from a P/P site to another P/P site, along the [110] direction, as depicted in Figure 1c. Given the five configurations on the V/VO side and three on the P/P side, there are 15 combinations of starting and ending configurations for the V/VO to P/P path. In this case too, when taking into account duplicative paths, there are15 combinations of starting and ending configurations for V/VO the V/VO path. Finally, there are six unique combinations for P/P the P/P path. We anticipate that the energy barrier for ferrocene diffusion will depend on the initial and final structures. Therefore, in this work, we analyze all thirty-six potential paths using CI-NEB calculations.

3. Discussion of Methods Validation

3.1 Optimizing CI-NEB Calculations for Ferrocene Diffusion.

CI-NEB calculations are known for being resource-intensive. To balance accuracy with resource utilization, two major factors must be considered: the number of images along the diffusion path and the k-mesh density. To determine suitable simulation conditions for calculations, we began with the simplest scenario, E-V-45º to E-V-45º, as shown in Figure 2a). To aid in understanding ferrocene diffusion, we have also created an animation, which can be found in the Supplementary Information (SI). We perform two calculations: one with 15 images (dense resolution), the other with 6 images (coarse resolution). The energy barriers and curves were nearly identical, leading us to conclude that 6 images are sufficient for our subsequent calculations. In particular, we note that the maximum in the energy is not at the mid-point of the path as we would expect for a simple molecule; we analyze this in more detail below. Similarly, in Figure 2b), the k-mesh densities of 2x2x3 and 4x4x5 yielded almost identical results. Therefore, based on these calculations, we concluded that a configuration of 6 images and a 2x2x3 k-mesh density is adequate. This approach is

considerably more cost-effective and less time-consuming than using 16 images and a 4x4x5 k-mesh.

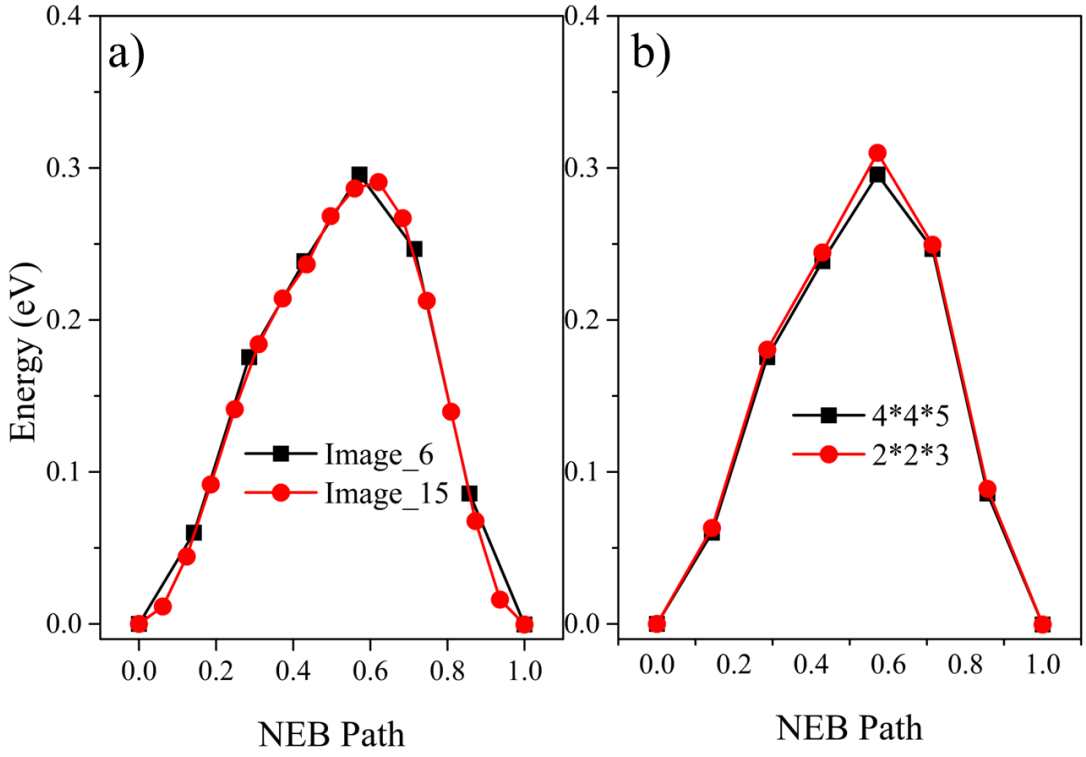

Figure 2. a) NEB calculation k-mesh density test on E-V-45º to E-V-45º Path: black for six images; red for 15 images; b) The NEB calculations with 4x4x5 (Red) and 2x2x3 (Black) K-mesh density.

3.2 Interactions of Ferrocenes.

In all of the calculations to this point, the host consists of a single $VOPO_4$ layer; meaning that with the periodic boundaries, the path of ferrocene diffusion is duplicated by periodic images above it and below it. However, in the real structure it is quite likely that the layers above and below do not have ferrocenes in these locations.

To address these issues, we consider a (computationally much more expensive) setup with two $VOPO_4$ layers, only one of which contains a ferrocene, as depicted in Figure 3a. For clarity, we call the structure in the left panel the single $VOPO_4$ layer and that in right panel the double $VOPO_4$ layer. This revised layering approach effectively

reduces the direct interaction between ferrocene layers by spacing them with multiple $VOPO_4$ layers.

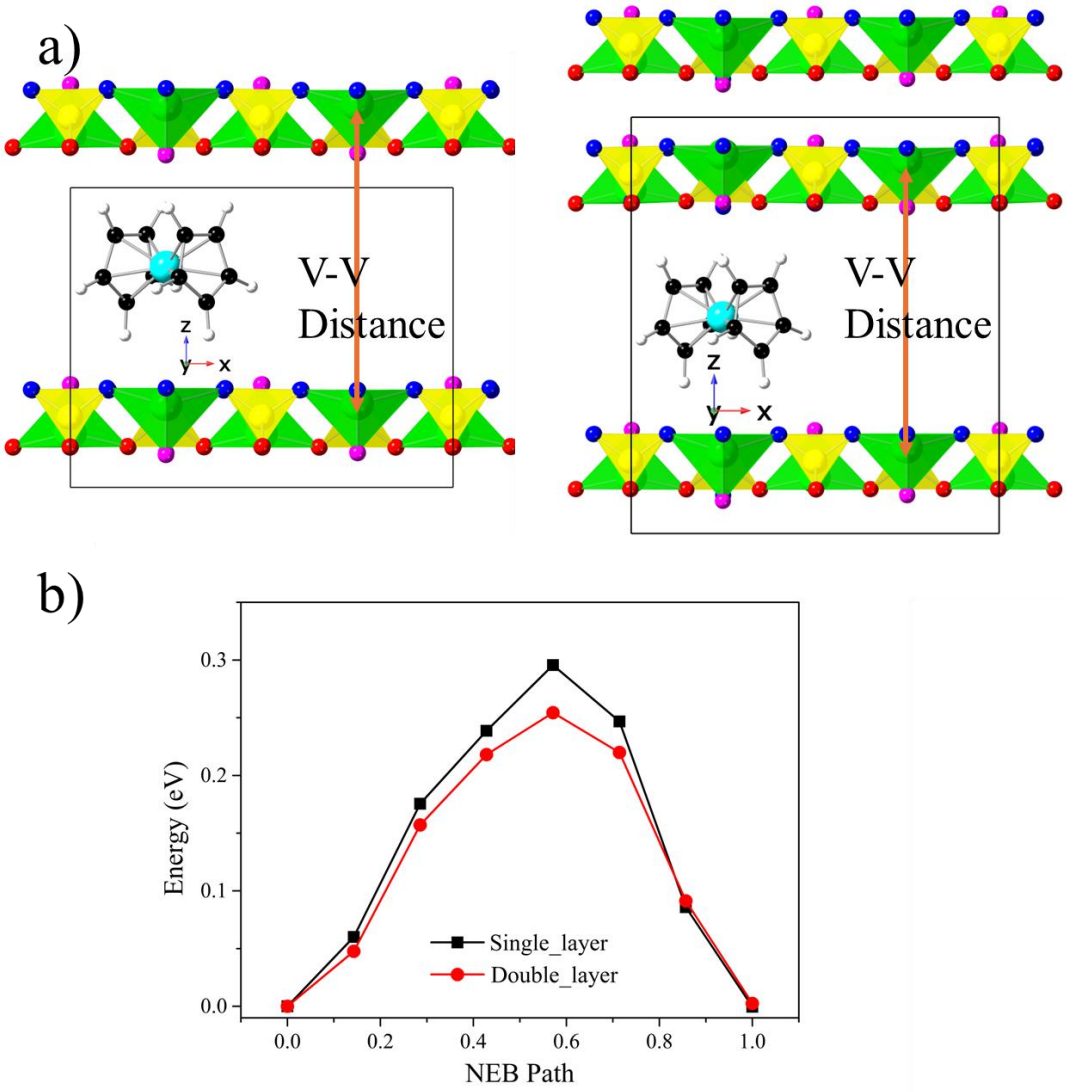

Figure 3. a) Depicts the two layering strategies for $VOPO_4$ and ferrocene along the c-axis, showcasing an alternating pattern designed to minimize direct interaction between ferrocene layers. The left panel illustrates a single layer of $VOPO_4$, while the right panel shows a double layer of $VOPO_4$. The black lines are the edges of the unit cells; (b) NEB energy profiles for pathways E-V-45º to E-V-45º.

Measurements of the V-V distances under both scenarios reveal significant insights. In single layer case, the V-V distances are constant at 9.67 Å, regardless of the presence of ferrocene. However, in the two-layer case, the V-V distance 10.038 Å in the layer occupied by the ferrocene and between 9.675 and 9.680 Å for the layer without the ferrocene. Interestingly, we found that the distortion of the $VOPO_4$ layer did not change significantly in calculations in both sections 3.1 and 3.2. Specifically, the V-O bond distances remain in the range of 1.91 to 1.98 Å, and the P-O bond distances are around 1.54 Å. The bond angle of V-O-P is approximately 132º. These values are consistent with those in pristine $VOPO_4$.[2,58] To illustrate this, we created a simple animation available in SI. Consequently, the subsequent discussion will focus on the distortion of the ferrocene.

We also calculate the energy barrier along the E-V-45º to E-V-45º transition path, as shown in Figure 3b, and find that the energy profile retains the same shape, with the energy barrier reduced by only 0.05 eV. Given these minor differences in energy, we choose to use the original model of alternating ferrocene and $VOPO_4$ layers. This decision is based on the observation that the slight reduction in energy does not significantly impact the overall energy profiles. Consequently, all subsequent NEB analysis is based on the single-layer simulation.

3.3 Characterizations of Ferrocene Deformation.

Considering the distinct stable configurations of ferrocene on the V/VO and P/P sides, it is evident that ferrocene must undergo structural changes during its diffusion. To characterize these changes, we use four measures:

1. the angle, τ, that the vector joining the center of the two cyclopentadienyl rings makes with the [010] direction in the (001) plane. This measures the rotation of ferrocene within this plane, see Figure 4a.

2. the angle, θ, between two -CH bonds in the two cyclopentadienyl rings, as highlighted in Figure 4b. θ = 0° corresponds to the eclipsed conformation; θ =

36° corresponds to the staggered conformation; an intermediate value of θ corresponds to a gauche conformation.

3. the dihedral angle, δ, between the cyclopentadienyl rings, providing insight into the tilting of the rings, see Figure 4c.

4. the angle, ϕ, between the apical -CH bonds form and the [001] direction. If ϕ changes, it indicates that the ferrocene is rolling; if ϕ doesn't changes, then the ferrocene is sliding as it moves. We label the -CH bonds on the two rings ϕ_1 and ϕ_2, see Figure 4d.

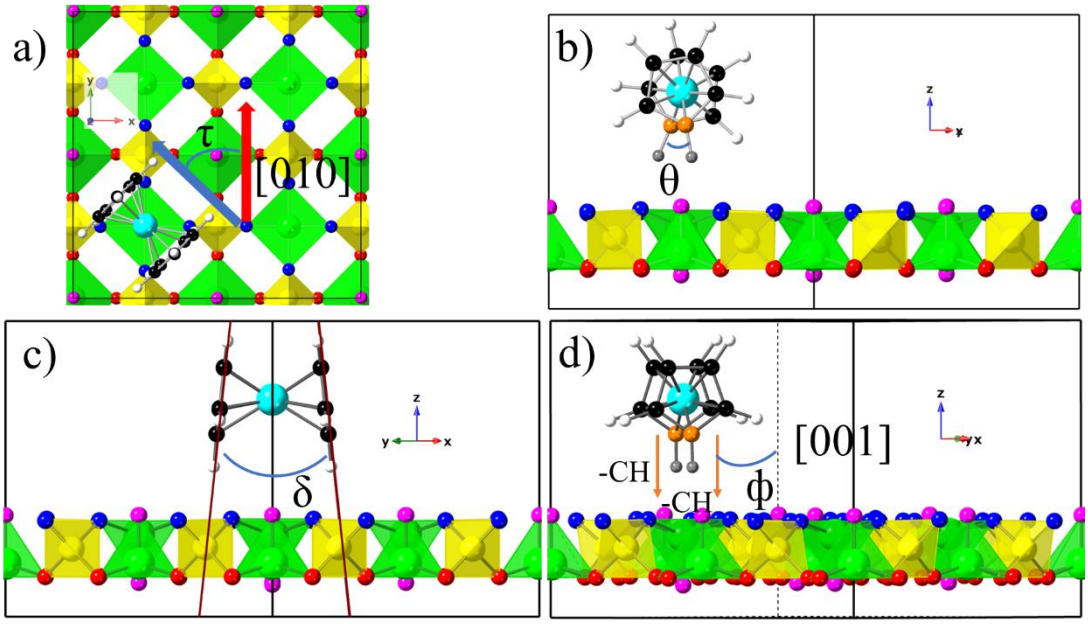

Figure 4. Schematics of a) the rotation angle, the blue arrow is the vector defined by ferrocene and the red arrow is the direction [010]; b) the angle between two -CH bonds. (highlighted with orange carbon and grey hydrogen atoms); c) the dihedral angle, with the red line indicating the plane formed by the cyclopentadienyl ring; d) the angle between the -CH bond and the [001] direction.

4. Ferrocene diffusion

4.1 From V to VO along [110] direction

Given the intricate nature of ferrocene diffusion, we characterize the fifteen potential pathways into four distinct groups based on the structural changes during diffusion:

Pure Sliding: This is the simplest diffusion process, with the ferrocene translating from point V to VO along the [110] direction without any observable rolling, rotation, or change in the relative orientations of the cyclopentadienyl rings.

Sliding with Rotation: This category includes instances where ferrocene exhibits rotational movement within the (001) plane during diffusion, indicating a departure from simple translational movement.

Sliding with Rolling: This category encompasses instances where ferrocene exhibits behavior characterized by the rolling of the cyclopentadienyl rings during diffusion, also indicating a departure from simple translational movement.

Sliding with Both Rotation and Rolling: This category represents a more complex diffusion mechanism, where ferrocene exhibits both rotational and rolling motions simultaneously.

4.2 Sliding only.

Our analysis identified three distinct pathways that demonstrate ferrocene undergoing sliding only simple translation, specifically from E-V-45º to E-VO-45º, from E-V-0º to E-VO-0º and S-V-45º to S-V-45º. To characterize the conformation of ferrocene along these pathways, we employed the four structural metrics outlined above. The energy profile and ferrocene conformations are detailed in Figure 5. Here, we show E-V-45º to E-VO-45º and E-V-0º to E-VO-0º as representative; S-V-45º to S-V-45º is shown in Figure S4 in the SI. We use the E-V-45º as the reference state because it has

the lowest total energy. Additionally, animations depicting the diffusion paths of these three processes have been included in the SI. These animations serve as a dynamic representation of ferrocene's simplified diffusion mechanisms, offering enhanced insight into its behavior during diffusion.

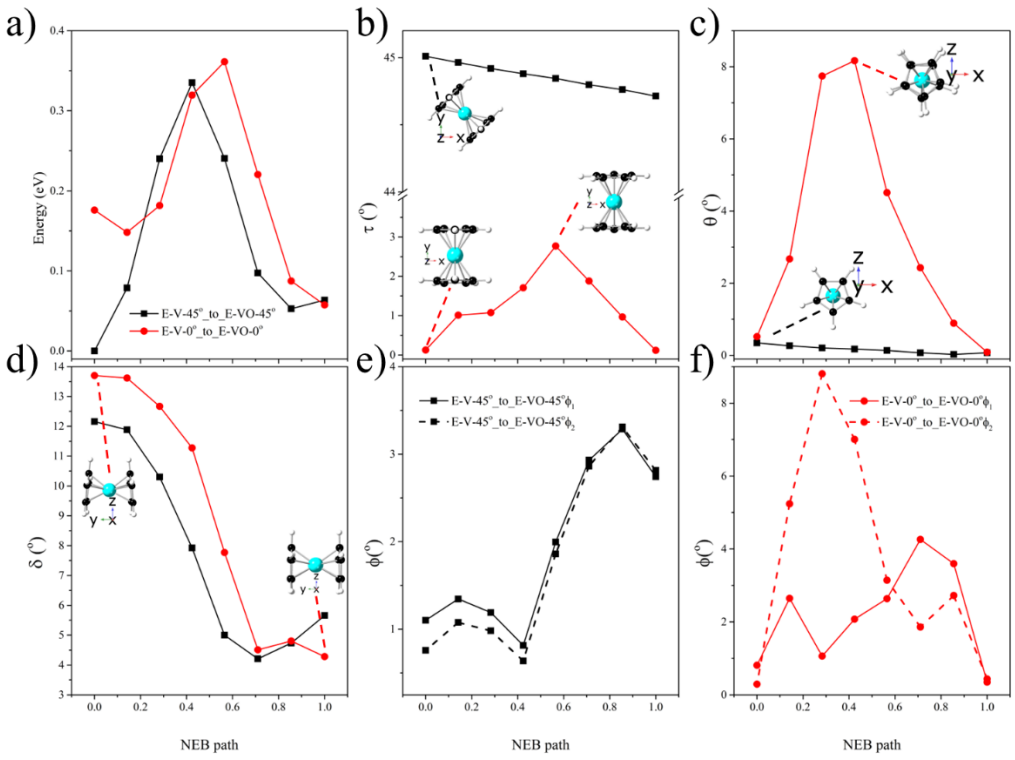

Figure 5. Structural analysis of ferrocene diffusion. (a) NEB energy profiles for pathways E-V-45º to E-VO-45º (black) and E-V-0º to E-VO-0º (red); (b) changes in rotational angle, τ, of ferrocene; note the different scales for the two sets of data; (c) changes in the angle, θ, between -CH bonds in the cyclopentadienyl rings; (d) evolution of dihedral angle, δ; (e) orientation of -CH bonds relative to the [001] direction for the E-V-45º to E-VO-45º path; solid line is ϕ_1 and dash line is ϕ_2. (f) orientation of -CH bonds relative to the [001] direction for the E-V-0º to E-VO-0º path. To depict the deformation of ferrocene, some of its relaxed structures are shown as insets.

From Figure 5a, the analysis of the two diffusion paths reveals that the energy barrier for E-V-45º to E-VO-45º (black) and E-V-0º to E-VO-0º (red) are 0.35 eV and 0.2 eV (red) relative to their starting positions. Ferrocene encounters a lower energy barrier along the red path relative to its end points compared to the black path relative

to its end points. However, these energy barriers are not directly comparable as the energies of the starting and ending points are not the same. To allow direct comparisons, the energy of the E-V-45º structure is selected as a uniform reference state for all other structures and diffusion paths because it has the lowest total energy. The Total Energy Barrier (TEB) is then the height of the barrier plus the difference in energy between the end points of a given structure and that of the E-V-45º structure. For cases in which the energies of the end points are not the same, the barriers in the two directions are not the same; we report the higher value. Returning to the E-V-0º to E-VO-0º path, we see that the TEBs have similar values, approximately 0.35 eV, with that of the E-V-0º to E-VO-0º being slightly higher.

Since the structures are oriented in the same way at the starting and ending points of each of these paths, there is no crystallographic need for the ferrocene to rotate in the x-y plane. However, Figure 5b indicates that in the E-V-45º to E-VO-45º path, ferrocene shows a very slight rotation in the (001) plane throughout the diffusion path of less than 0.5 º. For the E-V-0º to E-VO-0º path, both the starting and end points are truly at 0 º; however, during the migration path, the ferrocene does rotate, reaching a maximum rotation of 2.5º at peak energy position. This difference in rotational behavior may contribute to the slight difference in the energy barriers. Interestingly, Figure 5c shows that ferrocene maintains an eclipsed conformation in the E-V-45º to E-VO-45º path, whereas it transitions into a gauche arrangement and then back to eclipsed in the E-V-0º to E-VO-0º path, as indicated by an angle (θ) peaking at close to 7º; see also, the structure in the inset.

In Figure 5d, both paths begin with a bent conformation in ferrocene, but as diffusion progresses from V to VO, the dihedral angle decreases, suggesting that the cyclopentadienyl rings tend to become more parallel. Figure 5e focuses on the E-V-45º to E-VO-45º path, where the angles between the -CH bonds and the [001] direction change simultaneously and minimally, suggesting only slight rolling (the rotation angle is small) and maintenance of the eclipsed arrangement (the difference between the two angles is small), as supported by Figure 5c.

To determine whether the relative amounts of sliding and rotation during the diffusion path, we need to compare the diffusion distance and rotation angle. For perfect sliding, the angle between the reference -CH bonds on each cyclopentadienyl ring and the [001] direction would remain constant throughout the diffusion process. By contrast, for perfect rolling, the ferrocene molecule would rotate such that the cyclopentadienyl rings roll along the surface, akin to a wheel rolling on a flat surface. In this case, the angle between the -CH bonds and the [001] direction would change significantly and continuously.

We calculate the circumference of the cyclopentadienyl ring and the diffusion distance, then determine how many rotations are needed for pure rolling. The cyclopentadienyl ring in ferrocene is typically assumed to be a regular pentagon with a radius of 2.293 Å (averaged from the middle points to the hydrogen atoms in the cyclopentadienyl rings). Thus, the circumference is 14.407 Å. The distance from the V to V site along the [110] direction in the (001) plane is 4.478 Å. Thus, the number of rotations for pure rolling is roughly 4.478 Å /14.407 Å =0.31. This means that for the ferrocene molecule to perfectly roll from one site to the other, it would need to rotate by approximately 112º. Given the actual small rotation angle observed in Figure 5e, it is clear that the ferrocene molecule primarily slides with minimal rolling during diffusion in on the E-V-45º to E-VO-45º path.

By contrast, although ferrocene has same orientation in the initial and final states in, Figure 5f reveals a difference in these angles along the E-V-0º to E-VO-0º path, with one angle, ϕ_1, following a similar evolution to that in the -V-45º to E-VO-45º path, while the other, ϕ_1 is higher, close to 10º, indicating more rolling of ferrocene during diffusion and consistent with the gauche arrangement seen in the middle of the path in Figure 5c.

4.3 Sliding + Rotation.

We identified two pathways where ferrocene displays both sliding and rotation simultaneously, specifically from E-V-45º to E-VO-0º and from E-V-0º to E-VO-45º.

Following the methodology previously established, we show the outcomes of these observations in Figure 6, with animations in the SI.

In Figure 6a, the observed relative total energy barriers for both pathways are approximately 0.35 eV. This finding aligns with the results discussed in Section 4.2, indicating a consistent barrier for ferrocene diffusion across these paths. More importantly, analysis of the red line reveals that the energy profile has its minimum at locations away from the initial and final states, indicating that these intermediate states represent positions of stability within the energy landscape. Figure 6b illustrates that ferrocene undergoes linear rotation within the (001) plane during diffusion. From the analysis presented in Figure 6c, it is evident that the deviation from the perfect eclipsed conformation is minimal, with the largest observed value being approximately 3°.

Furthermore, Figure 6d also demonstrates a decrease in the dihedral angle as ferrocene diffuses, implying a tendency for the cyclopentadienyl rings to become more parallel. In Figures 6e and 6f, the observed difference between the angles ϕ_1 and ϕ_2 is minor, and the magnitudes of these angles are relatively small, leading to the conclusion that negligible rolling occurs for these pathways.

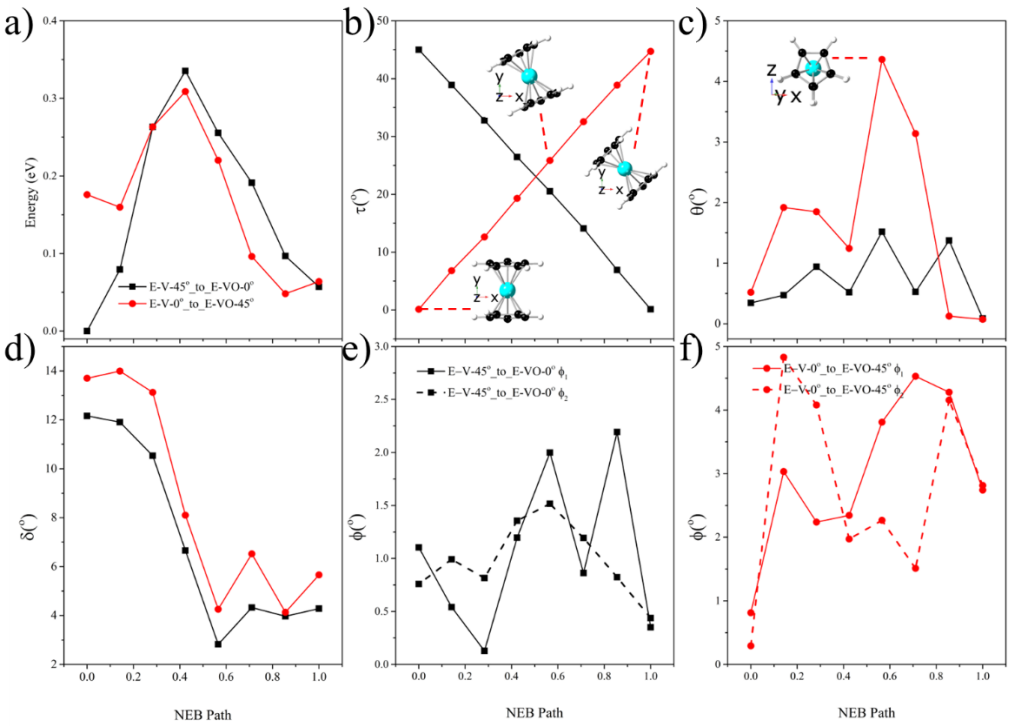

Figure 6. (a) NEB energy profiles for pathways E-V-45º to E-VO-0º (black) and E-V-0º to E-VO-45º (red); (b) rotational angle variations of ferrocene; (c) changes in the angle between -CH bonds in the cyclopentadienyl rings; (d) dihedral angle adjustments between the cyclopentadienyl rings; (e) orientation of -CH bonds relative to the [001] direction for the E-V-45º to E-VO-0º path; and (f) orientation of -CH bonds relative to the [001] direction for the E-V-0º to E-VO-45º path.

4.4 Sliding + Rolling.

In this section, our analysis expands to identify six distinct pathways where ferrocene exhibits both sliding and rolling. These pathways are E-V-0º to E-V-0º, E-V-45º to E-V-45º, E-V-45º to S-V-45º, E-VO-0º to E-VO-0º, E-VO-45º to E-VO-45º and E-VO-45º to S-V-45º.

Before delving into the specifics of ferrocene diffusion, an important aspect to consider is the direction of ferrocene's rolling during its passage through $VOPO_4$. To elucidate this, the E-V-45º to E-V-45º pathway was analyzed as a representative example. Our analysis encompassed both clockwise rolling (that is, in the same

direction as the sliding) and anti-clockwise rolling (in the opposite direction as the sliding) of ferrocene, with the findings presented in Figure S5 in the SI. The results indicated that, regardless of the rolling direction, the energy barrier for ferrocene's rolling remains the same, and the overall energy pathway is independent of the direction of the rolling. For the sake of consistency in our subsequent analyses, we opted to focus on the clockwise rolling of ferrocene in all of calculations.

Following our established methodology, the outcomes of these observations are documented in Figure 7, and corresponding animations are available in the SI. Here, we don't discuss all of the characterizations in the manuscript, we only show the two typical paths, E-V-0º to E-V-0º, E-V-45º to E-V-45º. The others E-V-45º to S-V-45º, E-VO-0º to E-VO-0º, E-VO-45º to E-VO-45º and E-VO-45º to S-V-45º are shown in Figure S6 and S7 the SI.

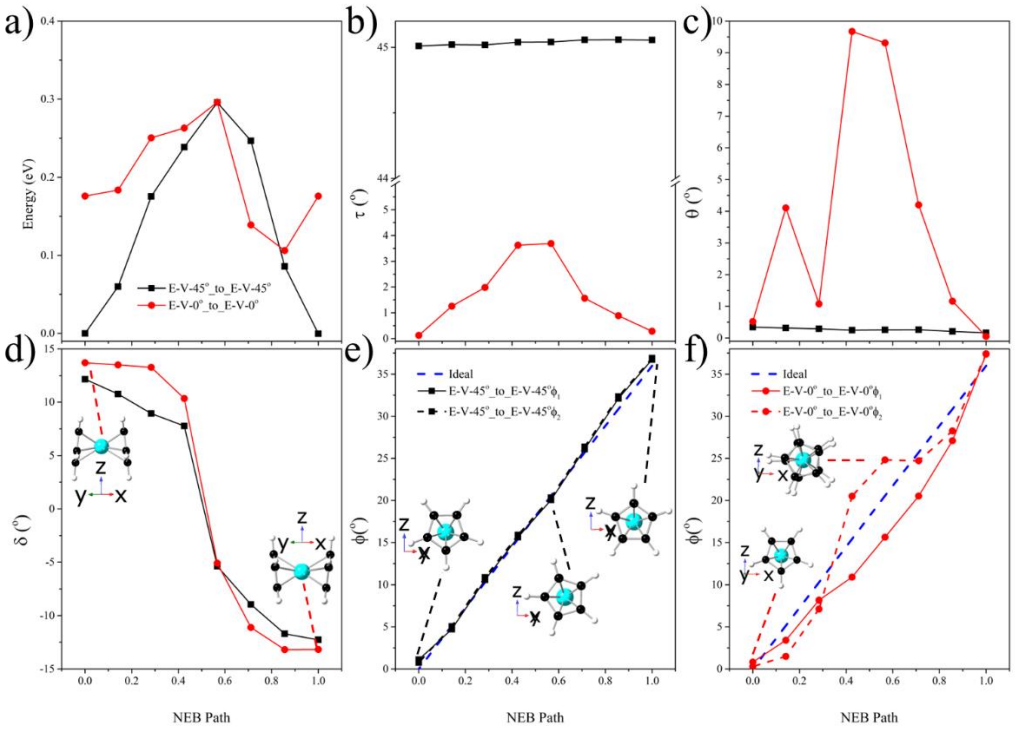

Figure 7. (a) NEB energy profiles for pathways E-V-45º to E-V-45º (black) and E-V-0º to E-V-0º (red); (b) rotational angle variations of ferrocene; (c) changes in the angle between -CH bonds in the cyclopentadienyl rings; (d) dihedral angle adjustments between the cyclopentadienyl rings; (e) orientation of -CH bonds relative to the [001]

direction for the E-V-45º to E-V-45º path, the blue dash line is the artificial linear rotation degree changed from initial to final; and (f) orientation of -CH bonds relative to the [001] direction for the E-V-0º to E-V-0º path.

In Figure 7a, the energy profiles for both the E-V-45º to E-V-45º and E-V-0º to E-V-0º diffusion paths exhibit peak energies around 0.3 eV. It is interesting that the asymmetry of the energy pathways despite the initial and final states having identical configurations. Figure 7b reveals that ferrocene maintains a consistent orientation in the (001) plane for both paths, with a small deviation, up to 5º, noted in the E-V-0º to E-V-0º path. This minor change suggests that orientation in the (001) plane is unlikely the primary factor influencing the energy profile. In Figure 7c, the conformation of ferrocene's aromatic rings in the E-V-45º to E-V-45º path remains eclipsed throughout, whereas a gauche arrangement is observed in the E-V-0º to E-V-0º path.

focuses on the dihedral angles of ferrocene, where positive angles indicate bending toward the -z direction and negative angles toward the +z direction, as shown in the inset. The asymmetry in the dihedral angles in Figure 7d observed in both profiles suggests changes in the bending of ferrocene along the diffusion path. A detailed NEB calculation for the E-V-45º to E-V-45º path, provided in Figure S8 in the SI, confirms this trend, highlighting differences in dihedral angles as another contributing factor to the energy profile asymmetry.

Figures 7e and 7f examine the rolling of the aromatic rings, highlighting deviations from a linear change in the rolling angle, as noted by the blue dashed line. Since the ferrocene rotation angle is 36º, which is much less than the rotation of 112º for pure rolling, this indicates that the ferrocene in both paths is a combination of rolling and sliding. In Figure 7e, the E-V-45º to E-V-45º path shows that both cyclopentadienyl groups roll almost continuously. Figure 7f shows that E-V-0º to E-V-0º has a more complex pattern of rolling, one ring initially rolling faster than the other, with the other catching up in the middle part of the path.

4.5 Sliding + Rotation + Rolling.

Our analysis reveals four distinct pathways where ferrocene exhibits simultaneous sliding, rotation, and rolling. These pathways are E-V-0º to E-V-45º, E-V-0º to S-V-45º, E-VO-0º to E-VO-45º, and E-VO-0º to S-V-45º. Following the methodology previously established, the outcomes of these comprehensive observations of E-V-0º to E-V-45º, E-V-0º to S-V-45º are documented in Figure 8, while E-VO-0º to E-VO-45º, and E-VO-0º to S-V-45º are shown in Figure S9 in the SI.

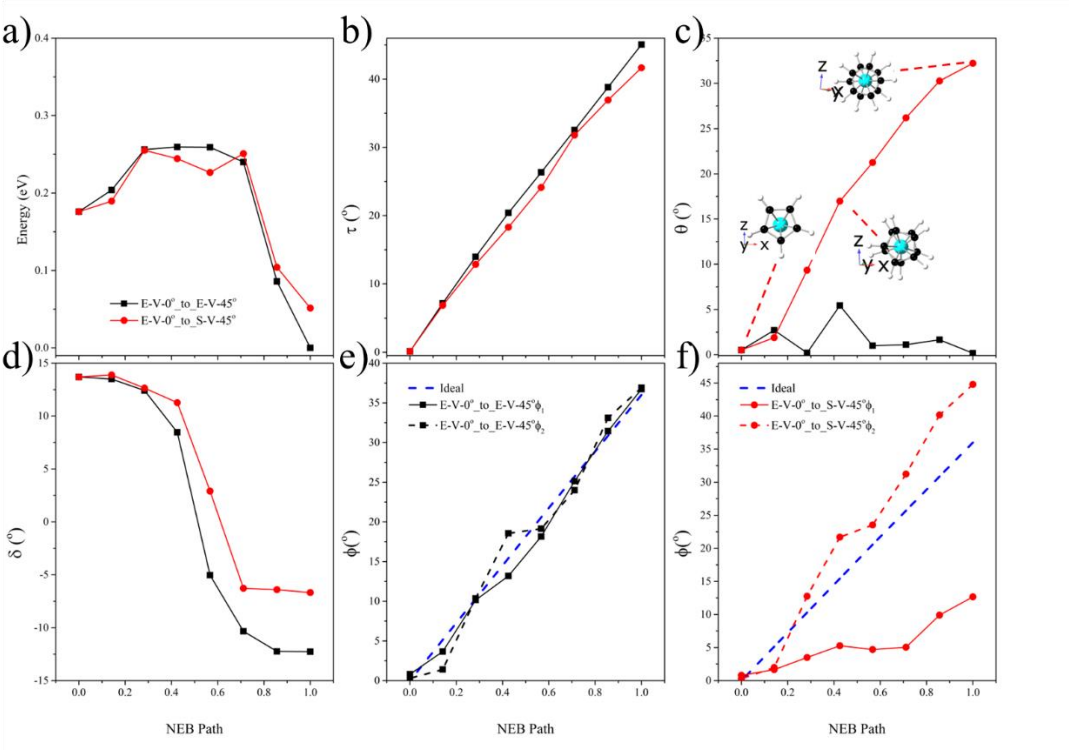

Figure 8. (a) NEB energy profiles for pathways E-V-0º to E-V-45º (black) and E-V-0º to S-V-45º (red); (b) rotational angle variations of ferrocene; (c) changes in the angle between -CH bonds in the cyclopentadienyl rings; (d) dihedral angle adjustments between the cyclopentadienyl rings; (e) orientation of -CH bonds relative to the [001] direction for the E-V-0º to E-V-45º path, the blue dash line is the artificial linear rotation degree changed from initial to final; and (f) orientation of -CH bonds relative to the [001] direction for the E-V-0º to S-V-45º path.

In Figure 8a, the NEB energy profiles for the diffusion pathways from E-V-0º to E-V-45º (black) and from E-V-0º to S-V-45º (red) are analyzed. Both pathways exhibit the relative total energy barrier of approximately 0.25 eV, which is notably lower than the energy barriers found in the preceding sections. A unique feature of the E-V-0º to E-V-45º sliding is the presence of an energy plateau in the middle of the NEB path, contrasting with the single peak energy barrier observed in other cases.

Figure 8b illustrates the linear variation in rotation degree for both pathways, transitioning smoothly from 0º to 45º. Figure 8c reveals that the ferrocene almost exclusively maintains an eclipsed arrangement in the E-V-0º to E-V-45º pathway. Conversely, in the E-V-0º to S-V-45º sliding, ferrocene shifts from an eclipsed through gauche arrangements to a staggered conformation, as show by the structures in the inset.

The analysis in Figure 8d shows the change in the dihedral angle direction from the -z axis towards the +z axis for both pathways, with the sliding from E-V-0º to S-V-45º exhibiting less severe bending compared to the E-V-0º to E-V-45º case. In Figure 8e, the angles ϕ_1 and ϕ_2 though not identical, follow a generally similar trend across both diffusion processes. However, Figure 8f for E-V-0º to S-V-45º highlights a growing disparity between ϕ_1 and ϕ_2 as diffusion progresses, indicating more complex dynamic changes, and consistent with the eclipsed to gauche to staggered conformation.

4.6. From P to P along [110] direction and From V to P along [100] direction.

Given the similarities in the analysis of the of diffusion from P to P along the [110] direction and from V to P along the [100] direction with the discussions presented in section 4.1, the detailed examinations and comparisons of these diffusion pathways are deferred to Figures S10 to S19 in the SI.

Briefly, we aim to focus on the most interesting case of the E-V-45º to G-P-20º path, as these start and end points represent the most stable sites at locations V and P, respectively. As Figure 9 shows, the relative total energy barrier for this path is only 0.11 eV, which is lower than those observed for all previously discussed pathways.

Interestingly, as depicted in Figure 9c, ferrocene exhibits a dynamic transition starting as an eclipsed structure and passing through intermediate gauche and eclipsed conformations, until finally settling in the gauche arrangement. This behavior is complemented by observations from Figures 9c and 9e, which highlight rapid changes in the orientation of the aromatic rings during the transition.

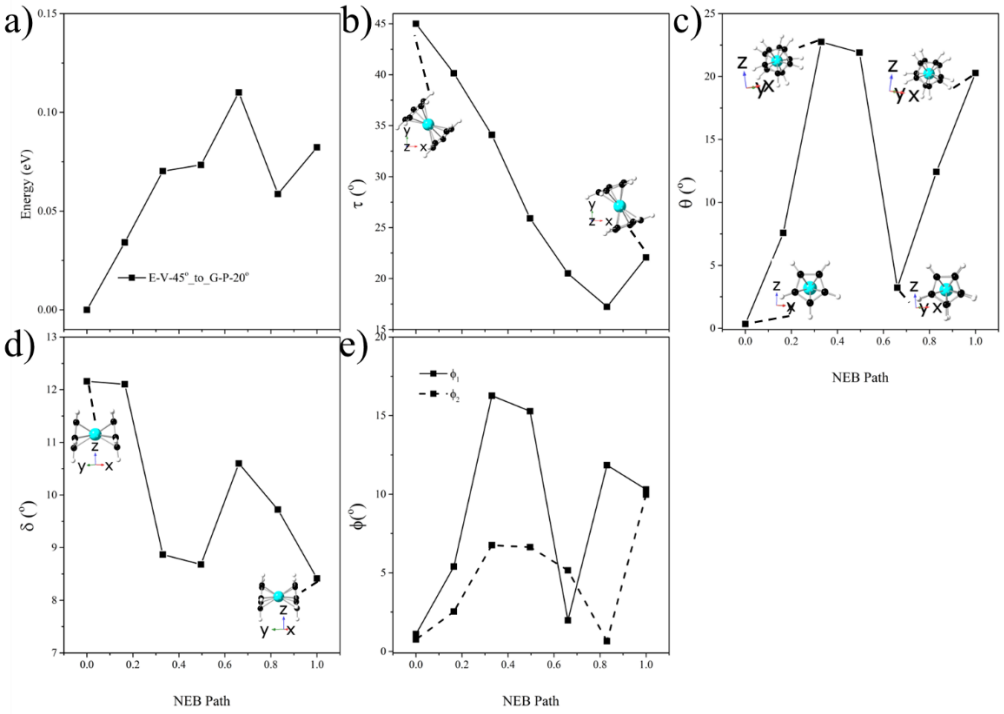

Figure 9. (a) NEB energy profiles for pathways E-V-45º to G-P-20º; (b) rotational angle variations of ferrocene; (c) changes in the angle between -CH bonds in the cyclopentadienyl rings; (d) dihedral angle adjustments; e) orientation of -CH bonds relative to the [001] direction for the E-V-45º to G-P-20º path.

4.7 Comparison of NEB Total Energy Barriers for Three Paths

To ascertain ferrocene's preferred diffusion direction, we analyzed the TEBs across all thirty-six potential pathways. This comparison in Figure 10 brings out significant variations across different scenarios.

In Figure 10a, for diffusion from one vanadium site to another, the TEBs range approximately between 0.25 eV to 0.36 eV. Figure 10b, for diffusion from one

phosphorous site to another, presents a similar situation with relative total energies of similar values. However, Figure 10c, for diffusion between as phosphorous and a vanadium site stands out, displaying a considerably lower energy range between 0.1 eV to 0.25 eV, with the majority of the pathways concentrated around 0.15 eV to 0.20 eV. Also, the lowest case is for E-V-45º to G-P-20º, with a TEB of 0.11 eV. Notably, the energy barrier is different when diffusing from the phosphorus site to the vanadium site in the opposite direction. Since the ferrocene on the phosphorus site has a higher total energy (+0.082 eV as mentioned in section 2.2), this transition presents an even lower barrier with 0.03 eV. Furthermore, these two configurations were also the lowest total energy configurations on V and P, respectively. Therefore, we conclude that the most likely diffusion path is from E-V-45º to G-P-20º, because from the energy perspective, this path has both the lowest total energy configurations and lowest energy barrier to diffusion.

Given the different energy barriers along various diffusion paths, we have consolidated our calculations and specifically show the most important in Figure 11. We identified the most stable configurations: E-V-45º and G-P-20º at the V and P sites respectively and presented the relative total energy barriers between these configurations in Figure 11. The energy barrier for diffusion from one V site to another along the [110] direction is 0.3 eV, and from one P site to another is 0.5 eV. In contrast, the energy barrier for diffusion from a V site to a P site is 0.11 eV, and from a P site to a V site is 0.03 eV. These energy profiles indicate a preferential diffusion pathway for ferrocene along the [100] or [010] direction from V to P sites; diffusion between these two sites thus allows long-range diffusion through the $VOPO_4$.

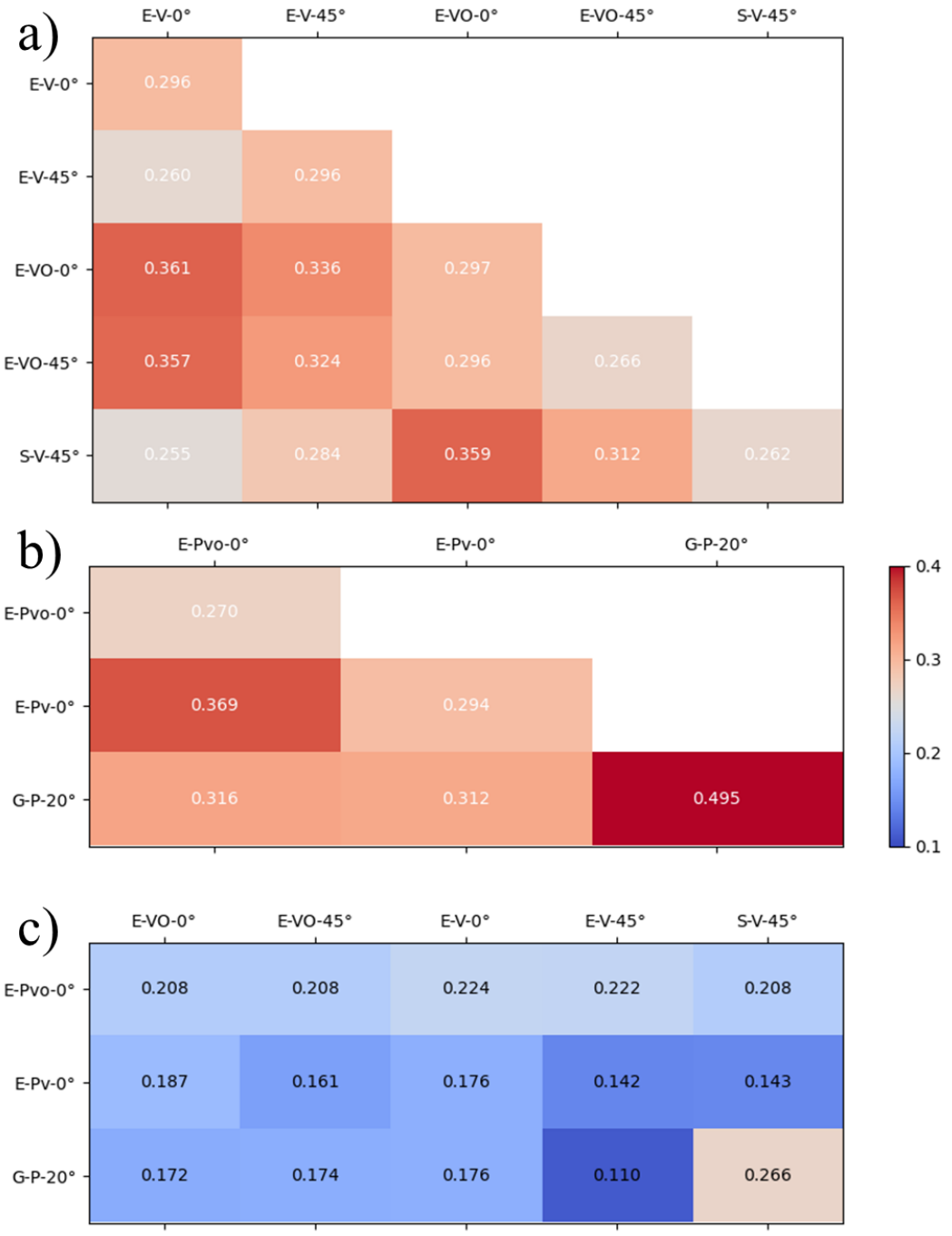

Figure 10. The total energy barriers of the total 36 possible NEB paths. a) from V to VO along [110] direction; b) from P to P along [110] direction and c) from V to P along [100] direction.

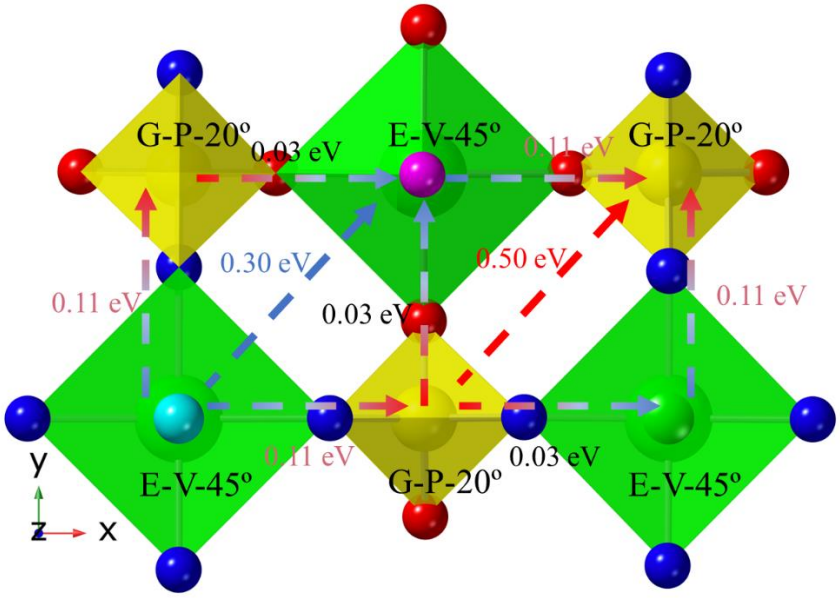

Figure 11. The total energy barriers for ferrocene diffusing through $VOPO_4$. The hydrogen and carbon atoms of ferrocene are omitted for clarity.

5. Conclusions.

In this study, the NEB method was employed to characterize the diffusion of ferrocene through $VOPO_4$. Acknowledging the sensitivity of NEB calculations to initial and final states, we leveraged our prior findings identifying five stable configurations on the V site and three on the P site. This foundational knowledge allowed the identification of 36 distinct diffusion pathways: 15 from V to VO along the [110] direction, 15 from V to P along the [100] and the [010] direction, and 6 from P to P also along the [110] direction. Subsequent NEB calculations revealed that the relative total energy barriers for ferrocene diffusion along the [110] direction span between 0.25 eV and 0.35 eV, surpassing those along the [100] direction, which range from 0.11 eV to 0.20 eV. This variance in energy barriers led us to identify a preference for ferrocene diffusion from V to P along the [100] direction. Notably, the pathway from E-V-45º to G-P-20º, characterized by the lowest energy barrier of 0.11 eV, and 0.03 eV in the opposite direction, correlates with the lowest total energy configurations at V and P

sites, respectively, suggesting its predominance in ferrocene diffusion through $VOPO_4$ at the atomic level.

Our exploration into the structural evolution of ferrocene as it diffuses through $VOPO_4$ introduced a set of four analytical measures to capture its conformational dynamics: the rotational angle of ferrocene within the (001) plane as measured against the [010] direction, the angular relationship between -CH bonds within the cyclopentadienyl rings, the dihedral angle defining the orientation of these rings with respect to each other, and the positioning of -CH bonds in alignment with the [001] direction. Utilizing these metrics allowed for the stratification of observed diffusion pathways into categories reflecting increasing levels of complexity. This ranged from simple translational movements, as observed in pathways like E-V-45º to E-VO-45º, to more complex behaviors involving rotation, exemplified by E-V-45º to E-VO-0º, and rolling, such as E-V-45º to E-V-45º. Additionally, pathways that exhibit both rotation and rolling, like E-V-0º to E-V-45º, were identified, further delineating the intricate conformational shifts experienced by ferrocene.

This systematic classification sheds light on the multifaceted structural transformations ferrocene undergoes during its diffusion journey. By highlighting the significance of these chosen metrics, we enhance the granularity of our understanding regarding ferrocene's conformational changes. This detailed characterization not only demystifies the complex diffusion mechanisms but also significantly contributes to our knowledge on the structural evolution of ferrocene, offering deep insights into its behavior within the $VOPO_4$ matrix.

In future research, the effect of applied pressure along the z-direction on the energy barrier for ferrocene diffusion should be investigated. Future studies will also incorporate the implicit solvation model[59–61] to more accurately simulate ferrocene diffusion, thus enhancing the realism of our computational approach. This work not only advances our understanding of ferrocene's diffusion mechanisms but also sets the stage for investigating the influence of external conditions on its behavior.

Conflicts of Interest Statement

The authors declare no conflicts of interest.

Data availability

Data for this article, including simulation results and raw data are available at Zenodo at https://doi.org/10.5281/zenodo.11465540.

Acknowledgments

This work was supported, in part, by the Division of Materials Research (DMR) at the National Science Foundation (NSF) via DMR-1904596 (D.R.T.). We acknowledge Yuchen Sun for calculating the dihedral angle of ferrocene.

CRediT author statement.

Yuan Liu: Conceptualization, Methodology, Software, Writing – Original Draft, Visualization; **An T. Ta:** Conceptualization, Supervision, Validation; **Seaton Ullberg:** Methodology, Validation; **Jiahui Liu:** Conceptualization, Investigation; **Daniel R. Talham:** Conceptualization, Writing - Review & Editing, Supervision; **Simon R. Phillpot:** Conceptualization, Validation, Writing - Review & Editing and Supervision.

References:

1 A. Davidson, G. Villeneuve, L. Fournes and H. Smith, Direct redox intercalation of ferrocene in α-VOPO4, *Mater. Res. Bull.*, 1992, **27**, 357–366.

2 H. Tietze, The crystal and molecular structure of oxovanadium(V) orthophosphate dihydrate, VOPO4,2H2O, *Aust. J. Chem.*, 1981, **34**, 2035.

3 L. Hong, L. Li, Y.-K. Chen-Wiegart, J. Wang, K. Xiang, L. Gan, W. Li, F. Meng, F. Wang, J. Wang, Y.-M. Chiang, S. Jin and M. Tang, Two-dimensional lithium diffusion behavior and probable hybrid phase transformation kinetics in olivine lithium iron phosphate, *Nat. Commun.*, 2017, **8**, 1194.

4 H. Shi, Z. Jia, W. Wu, X. Zhang, X. Liu and X. Sun, The Development of Vanadyl Phosphate Cathode Materials for Energy Storage Systems: A Review, *Chem. – A Eur. J.*, 2020, **26**, 8190–8204.

5 Y. Zhang, E. Huixiang Ang, Y. Yang, M. Ye, W. Du, C. Chao Li, Y. F. Zhang, Y. Yang, M. H. Ye, W. C. Du, C. C. Li and E. H. Ang, Interlayer Chemistry of Layered Electrode Materials in Energy Storage Devices, *Adv. Funct. Mater.*, 2021, **31**, 2007358.

6 R. Justinabraham, A. Durairaj, S. Ramanathan, A. Obadiah, R. John wesley, X. Lv and S. Vasanthkumar, Synthesis of porous g-C3N4 doped vanadyl phosphate for supercapattery application, *J. Energy Storage*, 2021, **40**, 102786.

7 B. Hu, C. Xu, D. Yu and C. Chen, Pseudocapacitance multiporous vanadyl phosphate/graphene thin film electrode for high performance electrochemical capacitors, *J. Colloid Interface Sci.*, 2021, **590**, 341–351.

8 L. Beneš, K. Melánová, J. Svoboda and V. Zima, Intercalation chemistry of layered vanadyl phosphate: a review, *J. Incl. Phenom. Macrocycl. Chem. 2012 731*, 2012, **73**, 33–53.

9 J. Zheng, T. Xu, G. Xia, W. Cui, Y. Yang and X. Yu, Water-Stabilized

Vanadyl Phosphate Monohydrate Ultrathin Nanosheets toward High Voltage Al-Ion Batteries, *Small*, 2023, **19**, 2207619.

10 K. J. Griffith and J. M. Griffin, in *Comprehensive Inorganic Chemistry III*, Elsevier, 2023, vol. 1–10, pp. 282–329.

11 J. Liao, Y. Han, Z. Zhang, J. Xu, J. Li and X. Zhou, Recent Progress and Prospects of Layered Cathode Materials for Potassium-ion Batteries, *ENERGY Environ. Mater.*, 2021, **4**, 178–200.

12 K. Zhu, Z. Sun, P. Liu, H. Li, Y. Wang, K. Cao and L. Jiao, Intercalation engineering of layered vanadyl phosphates for high performance zinc-ion batteries, *J. Energy Chem.*, 2021, **63**, 239–245.

13 H.-Y. Shi, Q. Jiang, T. He, W. Wu, S. Wang, X.-X. Liu and X. Sun, Uncovering and Retrieving the Internal Vanadium Migration Caused Voltage Fade in Vanadyl Phosphate Cathode for Aqueous Zinc Batteries, *ACS Energy Lett.*, 2023, **8**, 5215–5220.

14 H.-Y. Shi, Q. Jiang, W. Wu, Z. Lin, Z. Jia and X. Sun, Assisting Zn storage in layered vanadyl phosphate cathode by interactions with oligoaniline pillars for rechargeable aqueous zinc batteries, *Chem. Eng. J.*, 2023, **454**, 140323.

15 M. . Casaletto, S. Kaciulis, L. Lisi, G. Mattogno, A. Mezzi, P. Patrono and G. Ruoppolo, XPS characterisation of iron-modified vanadyl phosphate catalysts, *Appl. Catal. A Gen.*, 2001, **218**, 129–137.

16 Q. Wei, X. Tan, J. Zhang, L. Yang, L. Cao and B. Dong, Fe doped amorphous single layered vanadyl phosphate nanosheets as highly efficient electrocatalyst for water oxidation, *J. Colloid Interface Sci.*, 2021, **586**, 505–513.

17 G. Bagnasco, P. Galli, M. A. Larrubia, M. A. Massucci, P. Patrono, G. Ramis and M. Turco, in *Studies in Surface Science and Catalysis*, Elsevier, 2000, vol. 130, pp. 653–658.

18 F. Rüther, R. Machado, E. Gioria, S. L. Kunz, K. Wittich, P. Löser, M. Geske, S. A. Schunk, R. Glaum and F. Rosowski, Niobium Insertion into α II -VOPO 4 : Tuning the Catalytic Properties for Selective Oxidation, *ACS Catal.*, 2023, **13**, 3295–3307.

19 F. Puzzo, N. Capece, L. Setti, G. Pavarelli, J. De Maron, T. Tabanelli and F. Cavani, 1-Butanol dehydration and oxidation over vanadium phosphate catalysts, *Appl. Catal. A Gen.*, 2023, **661**, 119243.

20 M. Nakamura, The structure and the activity of vanadyl phosphate catalysts, *J. Catal.*, 1974, **34**, 345–355.

21 M. Faizan, Y. Li, R. Zhang, X. Wang, P. Song and R. Liu, Progress of vanadium phosphorous oxide catalyst for n-butane selective oxidation, *Chinese J. Chem. Eng.*, 2022, **43**, 297–315.

22 R. B. Smith, E. Khoo and M. Z. Bazant, Intercalation Kinetics in Multiphase-Layered Materials, *J. Phys. Chem. C*, 2017, **50**, 18.

23 A. Sood, A. D. Poletayev, D. A. Cogswell, P. M. Csernica, J. T. Mefford, D. Fraggedakis, M. F. Toney, A. M. Lindenberg, M. Z. Bazant and W. C. Chueh, Electrochemical ion insertion from the atomic to the device scale, *Nat. Rev. Mater. 2021 69*, 2021, **6**, 847–867.

24 C. F. Ferreira, E. E. Pérez-Cordero, K. A. Abboud and D. R. Talham, Reversible Medium-Dependent Solid–Solid Phase Transformations in Two-Dimensional Hybrid Perovskites, *Chem. Mater.*, 2016, **28**, 5522–5529.

25 Y. Zhu, Y. Ji, Z. Ju, K. Yu, P. J. Ferreira, Y. Liu and G. Yu, Ultrafast Intercalation Enabled by Strong Solvent–Host Interactions: Understanding Solvent Effect at the Atomic Level, *Angew. Chemie Int. Ed.*, 2019, **58**, 17205–17209.

26 N. A. Chernova, M. F. V. Hidalgo, C. Kaplan, K. Lee, I. Buyuker, C. Siu, B. Wen, J. Ding, M. Zuba, K. M. Wiaderek, I. D. Seymour, S. Britto, L. F. J.

Piper, S. P. Ong, K. W. Chapman, C. P. Grey and M. S. Whittingham, Vanadyl Phosphates AxVOPO4 (A = Li, Na, K) as Multielectron Cathodes for Alkali-Ion Batteries, *Adv. Energy Mater.*, 2020, **10**, 2002638.

27 M. S. Whittingham, C. Siu and J. Ding, Can Multielectron Intercalation Reactions Be the Basis of Next Generation Batteries?, *Acc. Chem. Res.*, 2018, **51**, 258–264.

28 D. Sun, M. Okubo and A. Yamada, Optimal water concentration for aqueous Li + intercalation in vanadyl phosphate, *Chem. Sci.*, 2021, **12**, 4450–4454.

29 M. Amedzo-Adore and J. I. Han, Chemically lithiated layered VOPO4 by a microwave-assisted hydrothermal method and its electrochemical properties in rechargeable Li-ion batteries and supercapacitor applications, *J. Alloys Compd.*, 2022, **911**, 165067.

30 F. Zhou, M. Cococcioni, K. Kang and G. Ceder, The Li intercalation potential of LiMPO4 and LiMSiO4 olivines with M=Fe, Mn, Co, Ni, *Electrochem. commun.*, 2004, **6**, 1144–1148.

31 Y. Wu, Q. Zong, C. Liu, Y. Zhuang, D. Tao, J. Wang, J. Zhang, Q. Zhang and G. Cao, Sodium-Ion Substituted Water Molecule in Layered Vanadyl Phosphate Enhancing Electrochemical Kinetics and Stability of Zinc Ion Storage, *Small*, 2023, **19**, 2303227.

32 X. Zhao, L. Mao, Q. Cheng, F. Liao, G. Yang and L. Chen, A new sodium ion preintercalated and oxygen vacancy-enriched vanadyl phosphate cathode for aqueous zinc-ion batteries, *J. Colloid Interface Sci.*, 2022, **627**, 1021–1029.

33 W. Yang, B. Wang, Q. Chen, Q. Zhao, Q. Zhang, S. Lu, Y. Gao, X. Wang, Q. Xie and Y. Ruan, Unravelling capacity fading mechanisms in sodium vanadyl phosphate for aqueous sodium-ion batteries, *J. Colloid Interface Sci.*, 2022, **627**, 913–921.

34 W. Yang, X. Wang, S. Lu, Y. Gao, T. Gao, T. Guo, Q. Xie and Y. Ruan,

Bimetallic Synergies Help the Application of Sodium Vanadyl Phosphate in Aqueous Sodium-Ion Batteries, *ChemSusChem*, 2023, **16**, e202202257.

35 S. Dilwale, M. Ghosh, V. Vijayakumar and S. Kurungot, Electrodeposited Layered Sodium Vanadyl Phosphate (Na x VOPO 4 · n H 2 O) as Cathode Material for Aqueous Rechargeable Zinc Metal Batteries, *Energy & Fuels*, 2022, **36**, 6520–6531.

36 R. Wei, Y. Lu, W. Ren, Y. Han, A. P. Vijaya Kumar Saroja, X. Xia, P. He, C. A. F. Nason, Z. Sun, J. A. Darr, J. Luo, M. Zhou and Y. Xu, Enhancing reversible Na-ion intercalation by introducing K-ions into layered vanadyl phosphate for sodium-ion battery cathodes, *J. Phys. Energy*, 2024, **6**, 025022.

37 Y. Zhu, Y. Qian, Z. Ju, L. Peng and G. Yu, Solvent-Dependent Intercalation and Molecular Configurations in Metallocene-Layered Crystal Superlattices, *Nano Lett.*, 2018, **18**, 6071–6075.

38 E. Rodríguez-Castellón, A. Jiménez-Ĺopez, M. Martínez-Lara and L. Moreno-Real, Intercalation of ferrocene and dimethylaminomethylferrocene into α-Sn(HPO4)2 · H2O and α-VOPO4 · 2H2O, *J. Incl. Phenom.*, 1987, **5**, 335–342.

39 G. Matsubayashi and S. Ohta, *Chem. Lett.*, 1990, 19, 787–790.

40 J. S. O. Evans, S. J. Price, H. V. Wong and D. O'Hare, Kinetic study of the intercalation of cobaltocene by layered metal dichalcogenides with time-resolved in situ X-ray powder diffraction, *J. Am. Chem. Soc.*, 1998, **120**, 10837–10846.

41 Y. Liu, A. T. Ta, R. S. Ullberg, J. Liu, D. R. Talham and S. R. Phillpot, Intercalation of ferrocene into vanadyl phosphate by density functional theory, *J. Mater. Chem. A*, 2024, **12**, 15472–15485.

42 G. Kresse and J. Hafner, *Ab initio* molecular dynamics for liquid metals, *Phys. Rev. B*, 1993, **47**, 558.

43 G. Kresse and J. Furthmüller, Efficient iterative schemes for ab initio total-energy calculations using a plane-wave basis set, *Phys. Rev. B*, 1996, **54**, 11169–11186.

44 J. P. Perdew, K. Burke and M. Ernzerhof, Generalized Gradient Approximation Made Simple, *Phys. Rev. Lett.*, 1996, **77**, 3865–3868.

45 P. E. Blöchl, Projector augmented-wave method, *Phys. Rev. B*, 1994, **50**, 17953.

46 G. Kresse and D. Joubert, From ultrasoft pseudopotentials to the projector augmented-wave method, *Phys. Rev. B*, 1999, **59**, 1758–1775.

47 S. L. Dudarev, G. A. Botton, S. Y. Savrasov, C. J. Humphreys and A. P. Sutton, Electron-energy-loss spectra and the structural stability of nickel oxide: An LSDA+U study, *Phys. Rev. B*, 1998, **57**, 1505.

48 B. Stahl and T. Bredow, Critical Assessment of the DFT + U Approach for the Prediction of Vanadium Dioxide Properties, *J. Comput. Chem.*, 2020, **41**, 258–265.

49 S. Grimme, J. Antony, S. Ehrlich and H. Krieg, A consistent and accurate ab initio parametrization of density functional dispersion correction (DFT-D) for the 94 elements H-Pu, *J. Chem. Phys.*, 2010, **132**, 154104.

50 W. Hujo and S. Grimme, Comparison of the performance of dispersion-corrected density functional theory for weak hydrogen bonds, *Phys. Chem. Chem. Phys.*, 2011, **13**, 13942.

51 D. M. Bylander, L. Kleinman and S. Lee, Self-consistent calculations of the energy bands and bonding properties of B12C3, *Phys. Rev. B*, 1990, **42**, 1394–1403.

52 M. P. Teter, M. C. Payne and D. C. Allan, Solution of Schrödinger's equation for large systems, *Phys. Rev. B*, 1989, **40**, 12255–12263.

53 G. Henkelman and H. Jónsson, Improved tangent estimate in the nudged elastic band method for finding minimum energy paths and saddle points, *J. Chem. Phys.*, 2000, **113**, 9978–9985.

54 G. Henkelman, B. P. Uberuaga and H. Jónsson, A climbing image nudged elastic band method for finding saddle points and minimum energy paths, *J. Chem. Phys.*, 2000, **113**, 9901–9904.

55 D. Sheppard, R. Terrell and G. Henkelman, Optimization methods for finding minimum energy paths, *J. Chem. Phys.*, 2008, **128**, 1–10.

56 E. a crystal and molecular structures program for Mac and Windows. CrystalMaker Software Ltd, Oxford, Images and video generated using CrystalMaker, www.crystalmaker.com.

57 V. Wang, N. Xu, J.-C. Liu, G. Tang and W.-T. Geng, VASPKIT: A user-friendly interface facilitating high-throughput computing and analysis using VASP code, *Comput. Phys. Commun.*, 2021, **267**, 108033.

58 T. M. Project, Materials Data on VPO5 by Materials Project, , DOI:10.17188/1193783.

59 K. Mathew, R. Sundararaman, K. Letchworth-Weaver, T. A. Arias and R. G. Hennig, Implicit solvation model for density-functional study of nanocrystal surfaces and reaction pathways, *J. Chem. Phys.*, 2014, **140**, 084106.

60 K. Mathew, V. S. C. Kolluru, S. Mula, S. N. Steinmann and R. G. Hennig, Implicit self-consistent electrolyte model in plane-wave density-functional theory, *J. Chem. Phys.*, 2019, **151**, 234101.

61 S. M. R. Islam, F. Khezeli, S. Ringe and C. Plaisance, An implicit electrolyte model for plane wave density functional theory exhibiting nonlinear response and a nonlocal cavity definition, *J. Chem. Phys.*, 2023, **159**, 234117.

Data Availability Statement

Data for this article, including simulation results, raw data, and analysis scripts, are available at Zenodo at https://doi.org/10.5281/zenodo.11465540.